An Improved Joint Optimization of Multiple Level Set Functions for the Segmentation of Overlapping Cervical Cells

Zhi Lu, Gustavo Carneiro, and Andrew P. Bradley, *Senior Member, IEEE*

Abstract—In this paper we present an improved algorithm for the segmentation of cytoplasm and nuclei from clumps of overlapping cervical cells. This problem is notoriously difficult because of the degree of overlap among cells, the poor contrast of cell cytoplasm and the presence of mucus, blood and inflammatory cells. Our methodology addresses these issues by utilising a joint optimization of multiple level set functions, where each function represents a cell within a clump, that have both unary (intra-cell) and pairwise (inter-cell) constraints. The unary constraints are based on contour length, edge strength and cell shape, while the pairwise constraint is computed based on the area of the overlapping regions. In this way, our methodology enables the analysis of nuclei and cytoplasm from both free-lying and overlapping cells. We provide a systematic evaluation of our methodology using a database of over 900 images generated by synthetically overlapping images of free-lying cervical cells, where the number of cells within a clump is varied from 2 to 10 and the overlap coefficient between pairs of cells from 0.1 to 0.5. This quantitative assessment demonstrates that our methodology can successfully segment clumps of up to 10 cells, provided the overlap between pairs of cells is below 0.2. Moreover, if the clump consists of three or fewer cells, then our methodology can successfully segment individual cells even when the overlap is around 0.5. We also evaluate our approach quantitatively and qualitatively on a set of 16 extended depth of field images, where we are able to segment a total of 645 cells, of which only around 10% are free-lying. Finally, we demonstrate that our method of cell nuclei segmentation is competitive when compared to the current state of the art.

Index Terms—Overlapping cell segmentation, Pap smear image analysis, Level set method

I. INTRODUCTION

The automated detection and segmentation of overlapping cells remains one of the most challenging problems in the analysis of microscopic images [13], such as those obtained from Pap smear [25]. The Pap smear is a screening test used to detect pre-cancerous and cancerous processes of the cervix. It consists of a sample of cells that are deposited onto a glass slide and further examined under a microscope (see Fig. 1(a)). The main factors affecting the sensitivity of the Pap smear test are the number of cells sampled, the overlap among these cells, the poor contrast of the cell cytoplasm, and the presence of mucus, blood and inflammatory cells [8]. These

Z. Lu and G. Carneiro are with the Australian Centre for Visual Technologies at the University of Adelaide, Australia, and A. P. Bradley is with the School of Information Technology and Electrical Engineering at The University of Queensland, Australia.

factors exacerbate both intra- and inter-observer variability and lead to a large variation in false negative results [23]. These issues have motivated the development of both automated cell deposition and slide analysis techniques. Cell deposition techniques, such as mono-layer preparations, remove a large portion of blood, mucus and other debris, reduce cell overlap and produce cells that are more likely to occur in a single focal plane. This makes both manual and automated slide analysis faster and easier [9]. Automated slide analysis techniques attempt to improve both the sensitivity and specificity of screening by automatically detecting, segmenting and then classifying individual cells present on a slide [11], [12], [13], [27], [43].

Clearly, the primary aim of both automated cell deposition and slide analysis techniques is to reduce the variability of screening by maximising the number of cells that can be accurately and unambiguously analysed, i.e., where both the nucleus and cytoplasm of each cell is clearly visible. Typically, normal and abnormal cells are distinguished based on the shape and size of both the nucleus and cytoplasm (and especially their ratio), plus photometric and textural properties of the nucleus [29]. However, a certain degree of overlap between cells is inevitable, even in well established monolayer preparation systems, such as ThinPrep [26]. Therefore, automated slide analysis techniques must be capable of analysing both free-lying and overlapping cells. In the conventional approach to cell analysis, where the cells are first segmented before features are extracted, this implies that the segmentation technique must be capable of both detecting and segmenting the nucleus and cytoplasm from overlapping cells.

The detection and segmentation of the nuclei and cytoplasm from cervical cells is a well studied problem [8], [10], [11], [12], [13], [28]. Current systems can segment the nucleus and cytoplasm of cervical cells in isolation [13] (i.e., cells without any overlap with other cells), segment overlapping nuclei [10], [11], [28] and segment overlapping nuclei plus the whole region representing the cellular clumps [8], [12], [14]. However, only recently has the complete segmentation of overlapping cells been addressed in cervical cytology [2], [20].

The automated detection and segmentation of overlapping cells is complicated by the fact that several layers of cervical cells are present on a glass slide (see Fig. 1(a)). This means that cells in an upper layer can partially obscure cells lying underneath [28]. In a manual examination, the cytologist uses the depth cue that focus provides in order to assist

in the interpretation of the overlapping cells. However, the separation of transparent layers from different focal depths is both a difficult and computationally intense task [38]. This is especially the case in cervical cytology, where the overlapping objects (cells) have poor contrast and are located at similar focal depths. Therefore, our proposed methodology analyses a single image with (digitally) extended depth of field (EDF), i.e., a single image where all objects are in focus [4]. This is a simpler and more efficient approach than analysing the original 3-dimensional 'stack' of images containing the overlapping cells.

In this paper, we propose an improved methodology capable of segmenting both the cytoplasm and nucleus of each individual cell in a clump of overlapping cervical cells. The main goal of our methodology is to produce a significantly larger number of fully segmented cells when compared to methods that only segment free-lying cells (i.e., isolated cells) [13]. Furthermore, the proposed segmentation of cells into nucleus and cytoplasm provides more information about the cells, as compared to the segmentation of nuclei only [10], [11], [28], or the segmentation of nuclei and cellular clump regions [8], [12]. The main advantage of having a larger number of fully segmented cells lies in the potential to improve the classification of cytologic specimens. The proposed methodology can be divided into two steps: an initial clump segmentation followed by a detailed segmentation of each individual cell. The first step consists of the following stages: i) cell clump detection using unsupervised classification [6], [39], ii) nuclei detection using the maximally stable extremal regions (MSER) algorithm [21] and iii) estimation of a shape prior for overlapping cell regions and an initial segmentation of each cell [37]. The second step then optimizes the initial segmentation using a level set methodology that utilises multiple level set functions to minimize an energy function [44]. This energy function is constrained by each individual cell's contour length [19], edge strength, shape prior [37], and the area of the overlapping regions between cells.

The main technical contribution of this paper is the energy formulation and the optimization strategy (second step above) that can deal with the problem of segmenting overlapping cervical cells using multiple level set functions (with one level set function per cell). In addition, we describe a database of manually segmented cervical cells that, for the first time, enables a systematic and unambiguous evaluation of both the detection and (complete) segmentation of overlapping cervical cells. In this database, the images are produced using real images of free-lying cells and background. Clumps of overlapping cells are then produced where the number of cells in a clump is varied from 2 to 10 and the overlap between pairs of cells is varied from 10% to 50%. Using this database, we explore the limitations of our approach and show that the proposed methodology can successfully segment cell clumps containing up to 10 cells provided that the overlap between pairs of cell is below 20%. Furthermore, the segmentation of cell clumps containing 2 to 3 cells is successful provided that the overlap is less than 50%. Note that we consider a successful segmentation to be one that detects at least 80% of the cells with an average Dice Coefficient larger than 0.9.

We further illustrate the efficacy our approach on a database of 16 real-world cytology images that contain manual annotations of both the nuclei and cytoplasm for all cells. Results show that our proposed technique for cell nuclei segmentation is on par with the current state of the art [8], with a Dice coefficient of 0.92. The importance of overlapping cell segmentation is supported by results in these 16 images which show that in these fields of view, there are a total of 645 cervical cells, of which only around 10% are free-lying and the remaining cells overlap with at least one other cellular object. In addition, the quantitative evaluation on this database demonstrates segmentation results that are consistent with those obtained on the synthetic database. Furthermore, results on this database are presented to qualitatively assess (i.e., by visual inspection) the segmentation of individual overlapping cells utilising the proposed methodology. The databases of synthetic and real cytology images together with ground truth annotation and Matlab code of the proposed segmentation algorithm will be made available to enable further research and benchmarking [1].

It should be noted that while an earlier version of this algorithm has previously been presented [20], this paper introduces a methodology that produces more accurate segmentation using the following extensions: 1) a new shape prior [37], based on the geometry of the detected nuclei and clumps, is described that produces more accurate constraints for the subsequent level set optimisation; 2) an updated formulation of the energy functional for the level set method is presented to specifically deal with the issue of poor contrast between cell clump and background; and 3) an expanded evaluation that includes a thorough and systematic quantitative assessment of the method utilising a carefully designed database of synthetically generated cell-clump images, which contains a varying number of cells and degree of cell overlap.

II. LITERATURE REVIEW

The methods described in the cervical cell segmentation literature have focused on four basic approaches [22]. The first and most traditional methods segment just the nuclei from isolated or partially overlapping cells. For example, [41] detects the boundary of nuclei by solving an optimal thresholding problem. Morphological analysis is also used to detect overlapping nuclei from cervical cell images [27]. There are also a number of nuclei segmentation methods for other types of cells. For instance, Hu *et al.* [35] propose a segmentation of esophageal cell nucleus with an improved snake. Cloppet an Boucher [34] use the watershed algorithm to segment overlapping nuclei of fibroblasts from Hutchinson-Gilford Progeria Syndrome. A comprehensive review for nuclei segmentation and classification can be found in [33].

The second approach explored in the literature is the segmentation of both the nucleus and cytoplasm from isolated (free-lying) cervical cells. For example, [43] adapt the gradient vector flow (GVF) [42] to cervical cell segmentation by estimating the orientation of the GVFs in the pixels near to an edge. The GVF is also explored in the detection of

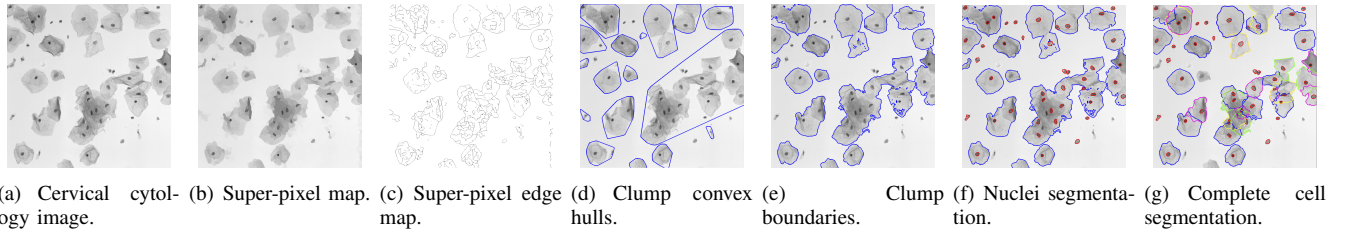| (a) Cervical cytology image. | (b) Super-pixel map. | (c) Super-pixel edge map. | (d) Clump convex hulls. | (e) Clump boundaries. | (f) Nuclei segmentation. | (g) Complete cell segmentation. |

Fig. 1. **(a)** Typical cervical cytology image; **(b)** Over-segmented super-pixel map generated by Quick Shift; **(c)** Super-pixel edge map; **(d)** Convex hull of each clump; **(e)** Accurate clump boundaries; **(f)** Nuclei detection and segmentation;**(g)** Overlapping cell segmentation of nucleus and cytoplasm.

nuclei and cytoplasm boundaries in a radiating fashion over the GVF field [13]. This second approach produces competitive results, but the fact that it only processes free-lying cells (and thus, a small percentage of the cells present on a typical cytology specimen) is a limitation that reduces the number of segmented cells per cytology specimen. The third approach focuses on the segmentation of overlapping nuclei and the boundaries of cell clumps. For example, [8], [12] propose a hierarchical approach, where the nucleus and cytoplasm candidates of the over-segmented cell images are merged into more meaningful regions by their spectral and shape properties. Finally they identify the nucleus and cytoplasm from these candidate regions through a classification process. Recently, Zhang *et. al.* [14] present a method, based on graph-cuts, that is able to delineate the boundary of a clump of cells and individual contours of overlapping nuclei from images of both normal and abnormal cervical cells. However, instead of providing accurate boundaries for each overlapping cell, these methods generate a contour of the whole clump of overlapping cells. Therefore this represents an improvement with respect to the other approaches presented above, but the fact that it only segments entire clumps instead of individual cells within the clumps is an issue that can limit the amount of information available for the classification of a cytologic specimen. In the above method, the detection of overlapping nuclei is facilitated by their homogeneous texture, ellipsoidal shape and high-gradient boundaries. Unfortunately, none of these characteristics can be associated with the segmentation of overlapping cytoplasm. Furthermore, some of the important features extracted from nuclei are based on optical density and texture, which may be adversely cross-contaminated when different nuclei overlap. To reduce the effect of this contamination, overlapping nuclei may still need to be de-focused in order to adequately separate them for further analysis [38].

The fourth approach focuses on the complete segmentation of individual cytoplasm and nuclei of overlapping cells. The methodology proposed in [2] is based on a locally constrained watershed transform. The results shown in that paper present limited evidence of the efficacy of the proposed technique. In particular, it is not clear the extent of cell overlap their methodology can successfully handle when segmenting the cytoplasm and nuclei of overlapping cells. Another methodology proposed is the one in [20], which is a preliminary version of the algorithm presented here. This method is based on an optimization involving several level set functions (each representing an individual cell within a clump) that interact with each other using both unary and pairwise terms. Here we present a number of extensions to that methodology, as described in Sec. I, and the results confirm that these extensions improve the accuracy of our previous approach.

In other types of microscopic images, the segmentation of overlapping cell images has also been explored. However, their extension to cervical cytology images is not straightforward because of the different challenges involved in each case. For instance, Wahlby *et al.* [40] use a watershed and a statistical analysis to segment multiple CHO-cells stained with calcein. A repulsive level set is proposed in [32] to segment breast tissue microarrays (TMAs), which are hematoxylin-stained. A sliding band filter is explored in [30] to segment overlapping cell nuclei and cytoplasm on the Drosophila melanogaster Kc167 dataset. Furthermore, Dufour *et al.* [31] present an active surface-based method to segment and track fluorescent cells in 3-D imaging. Although broadly relevant to our paper, these two works are applied to images where the cells present much smaller overlapping areas, when compared to typical cervical cytology images. Therefore, we believe that these approaches would require significant adaptation to be able to successfully deal with typical cervical cytology images.

Level set methods have been proven to be effective in numerous image segmentation tasks. Since its introduction by Osher [24], a number of variants have been proposed. For example, Wang *et. al.* [16] incorporate comprehensive pixel features into the level set method using a tensor representation. Gao *et. al* [15] propose an edge-based level set method to segment objects of interest in a relay fashion. Dambreville *et. al.* [17] represent the shape prior, which is used in the level set evolution, in feature space by kernel PCA and image domain by intensity. Recently, a DBN learned shape prior that contains global and local structures was introduced [18], which is used in a data-driven variational methodology. Finally, Yang *et. al.* [50][51] proposed a new level set method, in which the saliency morphorlogical map (SMM) is incorporated to generate the intial estimation that is close to the desired object.

III. METHODOLOGY

In this section, we first present the algorithm to build the EDF images analyzed, followed by a description of the proposed methodology for segmenting overlapping cervical cells.

A. Extended Depth of Field Image

Even when a mono-layer specimen preparation technique is used, cervical cells typically populate multiple focal planes, especially at high magnification. Therefore, we first acquire a 'stack' of images from multiple focal planes, before converting them to a single extended depth of field (EDF) image where all cellular objects are in focus. The advantage of this approach is that the scene segmentation, described below, need only be applied to a single EDF image rather than multiple images from different focal planes. Here, we use a computationally efficient one-pass algorithm based on the over-complete discrete wavelet transform [4]. In summary, this algorithm performs a wavelet transform on each image in the focal plane stack in turn to select the largest magnitude wavelet coefficient at each spatial location for each scale. It utilises a simplified contextual constraint based on the maximum coefficient amplitude in a local neighbourhood across all three orientation sub-bands and performs post-processing to ensure that all output pixel values lie within the same range as those in the original image stack. This algorithm was shown to produce EDF microscope images of superior quality when compared to the conventional discrete and complex wavelet transforms [4]. The acquisition process of the EDF images is shown in Fig. 2.

B. Scene Segmentation

Scene segmentation consists of three stages: i) the segmentation of cell clumps, ii) the detection and segmentation of nuclei, and iii) the estimation of the shape priors and initial segmentations of the cells required for the level set method, described in Sec. III-C. We provide details of these stages below.

1) Cell Clump Segmentation: The main goal of this first stage is to segment the cell clumps and remove the background, so that subsequent stages can concentrate on the regions containing cervical cells. This approach reduces the search space for the subsequent stages, since we can segment the individual nucleus and cytoplasm of the overlapping cells inside each clump (as compared to segmentation of the entire image).

The segmentation of cell clumps consists of a three-stage process. First, we run the quick shift algorithm [39] (a variation of mean shift [6]) to find local maxima of a density function that takes into account gray value similarities and spatial proximity. The outcome of this step is a map of super-pixels (see Fig. 1(b)) indicating the pixels linked to one of the local maxima found by quick shift. Each super-pixel is labeled with a gray value in the range $[0, 1]$, representing the mode of the gray values within that super-pixel. The second stage consists of running an edge detector on this super-pixel map, resulting in a reasonably clean edge map that detects the most prominent super-pixel edges, but removes most of the background information (see Fig. 1(c)). In order to find candidate cell clumps, the third stage consists of learning an unsupervised binary classification, where the classes are "background" and "cell clump." The initial assignment is provided by the edge map from the previous stage. Then connected components are found using a connected components

analysis [7] of the edge map and building a convex hull inside these components (see Fig. 1(d)). In this way, pixels inside a convex hull belong to the cell clump class and those outside belong to the background class. Using maximum likelihood estimation, we learn a Gaussian mixture model (GMM) for each class, where the features extracted from each pixel consists of its gray value. After learning these two models, we classify each pixel using the likelihood ratio between these two classes. Then, we take the result of this likelihood map and re-estimate the GMM of both classes and repeat this process util the GMM parameters are stable (in practice, we found that iterating this re-estimation process 10 times produces results that are consistent). As expected, this localized GMM-based classification produces noisy results in some areas of the imageand so a post-processing is applied involving a simple clustering algorithm that merges neighboring pixels that are classified as clump. This is followed by an elimination of clusters of size smaller than a preset threshold. A typical final result of this classification is presented in Fig. 1(e).

2) Nuclei Detection and Segmentation: The accurate detection and segmentation of nuclei is critical for our methodology since each nucleus represents a cell hypothesis that is then used to estimate a shape prior and an initial segmentation for the subsequent level set optimization. Nuclei can be characterized by relatively low gray values, homogeneous texture and well defined and almost circular borders. If we assume that the nuclei do not overlap, then we can use the Maximally Stable Extremal Regions (MSER) algorithm [21] using the previously obtained cell clumps as the input. The MSER algorithm is a method that detects stable connected components using a range of level sets of the image. Given the cell clumps as input, this algorithm will output "blobs" that represent the candidate nuclei. We then filter out some of these candidates by their appearance and shape properties (e.g., eccentricity, area, mean intensity of the "blob", and the area ratio between the "blob" and the cells clump it belongs). In the experimental section, we present quantitative results that show the effectiveness of the nuclei detection as compared to the state-of-the-art [8]

3) Initial Cell Segmentation and Shape Prior: Based on our observations, the majority of cytoplasm contours are located on pixels at the same relative distance from their associated nuclei. This inspired us to assume that pixels farther away from the geometric centroid of that cell (and inside the clump of overlapping cells) have a larger chance of being on the cytoplasm boundary. At this stage, we use the geometry of the detected nuclei and clumps to build a shape prior [37] that represents this assumption. This also provides an initial segmentation for each individual cell, as required for the level set optimization described next in Sec. III-C, and is one of the major contributions of this paper. The shape prior is built so that we have two types of attractors for the level set: the estimated boundaries of the clumps and individual cells; and two types of repellents: the background and the nuclei. After segmenting the input image (e.g., in Fig. 3(a)) into cell clumps and nuclei and assuming that each nucleus represents a single cell (see Fig. 3(b)), the next stage involve building the shape prior and initial segmentations as follows:

1) Associate each point of the clump boundary to the

a) Cervical Cytology Specimen   b) Acquisition Platform   c) Slide with Pap-stained Cells   d) EDF Generation
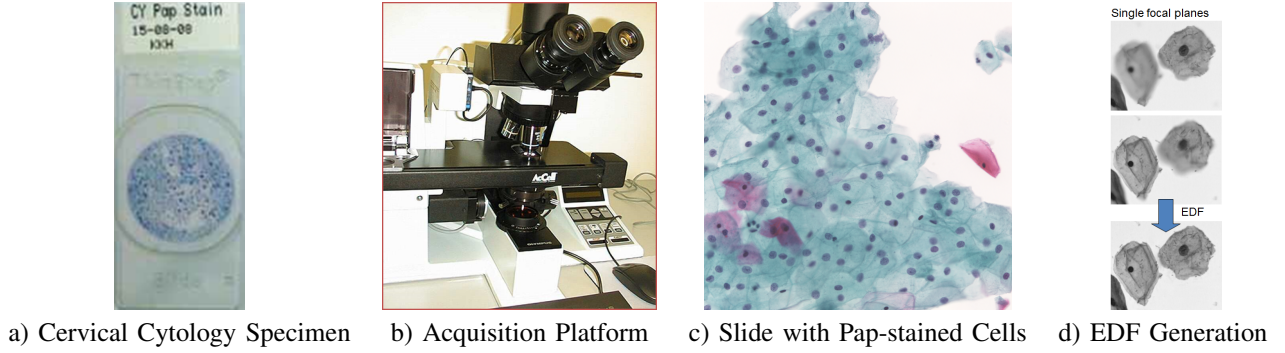
Fig. 2. The process of image acquisition uses a cervical cytology specimen in (a) and the acquisition platform in (b) to produce a stack of at least twenty focal plane images with a focal depth separation of $1\mu m$ (c), which are then converted into an EDF image (d), where all cellular objects are in focus.

nearest nucleus; this indicates a hypothesized cell ownership of that boundary point. The only constraint applied here is that the line connecting the clump boundary to the nucleus must be completely inside the clump (this implies that we are assuming that the cell region forms a convex set). In clumps containing a large number of cells, it may happen that some of the nuclei have no boundary associated with it (i.e., the cell is completely within the clump), so in this case the cell is assumed to be circular with radius equal to the distance to the nearest nucleus within the clump.

2) Extrapolate the cell boundary in each of the overlapping regions by following the extreme clump boundary points associated with that cell. For example, notice in Fig. 3(c) that the orange polygon represents the overlapping region between the two cells, and Fig. 3(d) shows the extrapolated cell boundaries achieved by interpolating the clump boundary points between the extreme points. The interpolation operation is performed by `TriScatteredInterp()`, a Matlab built-in function based on linear interpolation [45];

3) Compute the geometric centre of each cell, using the extrapolated cell boundaries obtained in step (2) above (see Fig. 3(e)). This boundary is then used as the initial cell segmentation for the level set optimisation;

4) For each cell indexed by i, use the boundaries estimated above to compute the individual shape prior as follows:

$$h_i(\mathbf{x}) = \begin{cases} 1 & \text{, if } \mathbf{x} \text{ outside clump } \mathcal{C} \\ \frac{-2}{1+\exp\{-\beta t(\mathbf{x})\}} + 2 & \text{, if } \mathbf{x} \text{ inside cell } i \\ 0 & \text{, otherwise} \end{cases},$$

(1)

where the set $\mathcal{C} = \{h_i\}_{i=1}^{|\mathcal{C}|}$ represents a clump with $|\mathcal{C}|$ cells denoted by h_i, the function $t(.)$ computes the distance between the point $\mathbf{x}$ on the image domain Ω and the geometric centre of the initial segmentation for cell i from step (3) above, β is a free parameter that is estimated via cross-validation, as explained in Sec. V. The first condition in (1) indicates that the point $\mathbf{x}$ is outside the clump boundary, the second condition denotes that the point $\mathbf{x}$ is inside the cell i boundary, and the last condition indicates the case where the point $\mathbf{x}$ is inside the clump $\mathcal{C}$ but outside the cell i boundary. The

shape prior constraint for each clump is then defined by (see Fig. 3(f)):

$$h_{\mathcal{C}}(\mathbf{x}) = \max_{h_i \in \mathcal{C}} h_i(\mathbf{x}).$$

(2)

C. Joint Level Set Segmentation of Overlapping Cells

The joint level set optimization introduced in this section represents another major contribution of this paper and uses as input the initial segmentation and shape prior previously described in Sec. III-B3. Consider that $\phi(x,y,t) : \Omega \to \mathbb{R}$ denotes a 2-D time dependent level set function (LSF) (Ω represents the image domain), and that N cells have been detected, then the set of LSF's that are available is denoted by $\{\phi_i\}_{i=1}^N$. The energy functional to be minimized is defined as:

$$\mathcal{E}(\{\phi_i\}_{i=1}^N) = \sum_{i=1}^N \mathcal{E}_u(\phi_i) + \sum_{i=1}^N \sum_{j \in \mathcal{N}(i)} \mathcal{E}_b(\phi_i, \phi_j), \quad (3)$$

where $\mathcal{E}_u(.)$ denotes the unary energy functional defined for each LSF independently, $\mathcal{E}_b(.,.)$ represents the binary function defined over pairs of LSF's, and $\mathcal{N}(i)$ represents the level set functions ϕ_j such that their zero level set intersects the zero level set of ϕ_i. The unary functional is defined by:

$$\mathcal{E}_u(\phi_i) = \mu \mathcal{R}(\phi_i) + \kappa \mathcal{D}(\phi_i), \quad (4)$$

where $\mu > 0$, $\kappa \in \mathbb{R}$, the first term is a regularization term that maintains the signed distance property $|\nabla \phi_i| = 1$ [19] and is defined as:

$$\mathcal{R}(\phi_i) = \int_\Omega p(|\nabla \phi_i|)d\mathbf{x}, \quad (5)$$

where $p : [0, \infty) \to \mathbb{R}$ is a potential function (e.g., $p(s) = 0.5(s-1)^2$ [19]),

$$\mathcal{D}(\phi_i) = \int_\Omega h_C(\mathbf{x})g\delta(\phi_i)|\nabla \phi_i|d\mathbf{x}, \quad (6)$$

where $h_C(\mathbf{x})$ is the shape prior constraint [37] for a clump representing the global features of pixels defined in (2), which assumes that the pixels inside the cell clump have a larger chance of being located on the cytoplasm boundary if they are located farther away from its associated nuclei. Here $g = \frac{1}{1+|\nabla G_\sigma * I|}$ shows smaller values of edge information than those of non-edge pixels, which represents the local
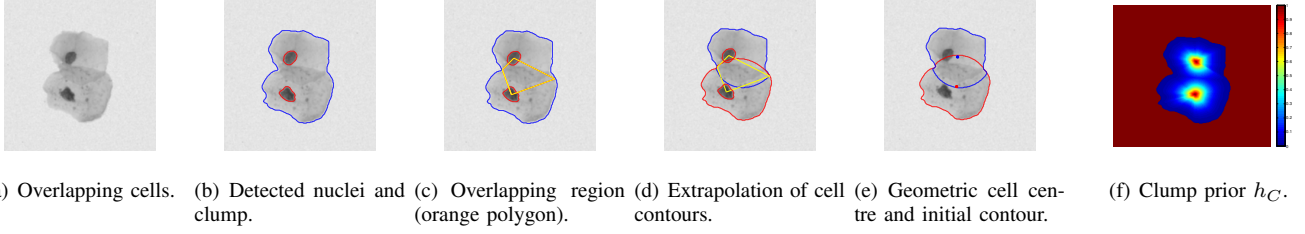
(a) Overlapping cells.   (b) Detected nuclei and clump.   (c) Overlapping region (orange polygon).   (d) Extrapolation of cell contours.   (e) Geometric cell centre and initial contour.   (f) Clump prior h_C.

Fig. 3. **(a)** Illustration of an overlapping cell image; **(b)** Cell clump and nuclei detected from the image; **(c)** Association of contour points from the clump to cell nuclei; **(d)** Extrapolation of cell boundary in the overlapping region; **(e)** Geometric cell center and new extrapolation; and **(f)** Binary constraint h_C, where red denotes values close to one and blue values close to zero.

features ($I : \Omega \to \mathbb{R}$ denotes the image and G_σ the Gaussian kernel with standard deviation σ), $\delta(.)$ represents the Dirac delta function. The unary term $\mathcal{D}(\phi_i)$ is derived from the length term of the geodesic active contour (GAC) proposed by Caselles *et al.* [49], as suggest by [19]. Note that we keep the term $|\nabla\phi|$ to maintain compatibility with the literature. But it could be removed because the regularization in [19] guarantees $|\nabla\phi| = 1$. Equation (6) is minimized when the shape of the cell is similar to the prior $h_C(\mathbf{x})$ and the zero level set of ϕ_i is located at places in the image I with large gradient.

The binary functional in (3) is defined as:

$$\mathcal{E}_b(\phi_i, \phi_j) = \chi \int_\Omega h_C(\mathbf{x}) g H(-\phi_i) H(-\phi_j) d\mathbf{x}, \qquad (7)$$

where $\chi > 0$, $H(\cdot)$ is the Heaviside function, and $h_C(\mathbf{x})$ is the binary shape prior (2). This binary functional is minimized when the intersection of the non-positive regions of the level set functions ϕ_i and ϕ_j has a small area, contains regions of $h_C(\mathbf{x})$ with low values (i.e., close to the borders between cell and background and far from nuclei) and comprises as many image regions with large gradient as possible (indicating the presence of edges between the two cells). For the special case $g = 1$, the shape prior is not considered (i.e., $h_C(\mathbf{x}) = \mathbf{1}$) and the binary term exactly represents the area of the overlapping region.

The gradient flow for minimizing the energy functional $\mathcal{E}(\{\phi_i\}_{i=1}^N)$ in (3) is based on finding the steady state solution of the gradient flow equation [1] for each LSF $\phi_i(x, y, t)$, as follows:

$$\frac{\partial \phi_i}{\partial t} = -\frac{\partial \mathcal{E}(\{\phi_i\}_{i=1}^N)}{\partial \phi_i}, \qquad (8)$$

where $\frac{\partial \mathcal{E}(\{\phi_i\}_{i=1}^N)}{\partial \phi_i}$ is the Gâteaux derivative of the functional $\mathcal{E}(\{\phi_i\}_{i=1}^N)$. The evolution in (8) follows the steepest direction of the functional $\mathcal{E}(\{\phi_i\}_{i=1}^N)$, which is represented by $-\frac{\partial \mathcal{E}(\{\phi_i\}_{i=1}^N)}{\partial \phi_i}$ for each LSF ϕ_i. The level set function used in this paper is basd on DRLSE [19], which is implemented with a finite difference scheme and the time step $\Delta t > 1$ is used to speed up curve evolution. Based on (3) and using the linearity of the Gâteaux derivative, we have:

$$\frac{\partial \mathcal{E}\{\phi_i\}_{i=1}^N}{\partial \phi_i} = \frac{\partial \mathcal{E}_u(\phi_i)}{\partial \phi_i} + \sum_{j \in \mathcal{N}(i)} \frac{\partial \mathcal{E}_b(\phi_i, \phi_j)}{\partial \phi_i}, \qquad (9)$$

for all cells represented by $i \in \{1, ..., N\}$. The derivative of

the unary energy term in (9) is computed as follows:

$$-\frac{\partial \mathcal{E}_u}{\partial \phi_i} = \mu \mathrm{div}(d_p(|\nabla\phi_i|)\nabla\phi_i) + \kappa\delta_\varepsilon(\phi_i)\mathrm{div}\left(h_C g \frac{\nabla\phi_i}{|\nabla\phi_i|}\right), \qquad (10)$$

where $d_p(x) = p'(x)/x$ (with $p(.)$ defined above in (5)), $\mathrm{div}(.)$ is the divergence operator, and $\delta_\varepsilon(x) = (1/(2\varepsilon))(1 + \cos(\pi x/\varepsilon))$ for $|x| \leq \varepsilon$ and $\delta_\varepsilon(x) = 0$ otherwise (with $\varepsilon = 1.5$ [19]). Finally, the derivative of the binary term is given by:

$$-\frac{\partial \mathcal{E}_b(\phi_i, \phi_j)}{\partial \phi_i} = \chi \left(h_C g \delta_\varepsilon(\phi_i) H(-\phi_j)\right). \qquad (11)$$

If ϕ_i and ϕ_j do not intersect during the level set evolution, then $-\frac{\partial \mathcal{E}_b(\phi_i, \phi_j)}{\partial \phi_i} = 0$.

The full algorithm proposed in this paper is outlined in Table I, where the minimization of (9), represented by step 9 in the algorithm, follows a sequential schedule from cells 1 to N.

IV. MATERIALS AND EXPERIMENTS

The dataset utilised in this paper consists of 16 non-overlapping fields of view (FOV) images obtained from four cervical cytology specimens. Each FOV consists of between 20 and 60 Papanicolaou stained cervical cells with varying degrees of overlap, and distributed on average in 11 clumps with 3.6 cells per clump, where the clump size varies from 1 to 21 cells. The specimens were prepared using the AutoCyte PREP technology [3] and so each specimen is around $20\mu m$ 'thick' in the focal-dimension. Images were acquired on an Olympus BX40 microscope with a ×40 objective and a four mega-pixel SPOT Insight camera, with square pixels of size of $7.4\mu m$ and a 100% fill factor. This gives an image resolution of around $0.185\mu m$ per pixel. The ×40 objective has a numerical aperture of 0.75, which gives a depth of field of approximately $1\mu m$. Therefore, for each FOV, a stack of at least twenty focal plane images were acquired with a focal depth separation of $1\mu m$. Each FOV image was then converted to an EDF image as described in Sec. III-A.

We assess the performance of our proposed methodology both quantitatively and qualitatively. The quantitative assessment consists of three experiments: the first one assesses the limitations of our methodology systematically using a comprehensive dataset of synthetically generated images containing

TABLE I
ALGORITHM FOR THE SEGMENTATION OF OVERLAPPING CELLS

Pseudo-code
Input: Cytology specimen
Output: Individual cytoplasm and nucleus contours of overlapping cervical cells
Stage 0 - Construction of EDF cytology image I
Stage 1 - Scene segmentation
1   Compute super-pixel map from I using Quick Shift
2   Compute gradient map from super pixels
3   Compute convex hull from gradient map to initialize clump and background GMM models
4   **while** clump and background GMM models not stable
5   Re-estimate clump and background GMM models
6   **end**
7   Post-processing to eliminate noise in clumps and clumps of size smaller than a preset threshold
8   Detect and segment nuclei using blobs represented by MSER (assume that N nuclei are detected at this stage)
9   Compute the initial segmentations for the cells $i \in \{1, ..., N\}$, and the shape priors, h_C (2).
Stage 2 - Joint Level Set for overlapping cell segmentation
10    $\{\phi_i^*\}_{i=1}^N = \arg\min_{\{\phi_i\}_{i=1}^N} \mathcal{E}(\{\phi_i\}_{i=1}^N)$ (3)
11   Re-compute h_C (2) using $\{\phi_i^*\}_{i=1}^N$ as the new initial segmentation for each of the N cells and iterate 10-11 until reaching a local minimum. Cell contours are the zero level sets of ϕ_i^*, for $i \in \{1, ..., N\}$.

a varying number of cells with differing degrees of overlap; the second experiment quantifies performance on a subset of 16 real EDF images; the last experiment measures the performance of nuclei detection and segmentation methodology on these 16 EDF images. The qualitative evaluation consists of a visual inspection of the segmentation results produced by our algorithm on the 16 EDF images.

For the systematic assessment, we first divide the 16 EDF images into a training set consisting of 4 images and a test set with 12 images (i.e., no overlap between the test and training images). Initially, all of the cervical cell nuclei, that were not touching the edge of the EDF image, were manually delineated by an experienced cytotechnologist. In addition, from the 4 training images, we manually delineated the cytoplasm of 12 isolated cervical cells (i.e., free-lying cells that do not overlap with other cells). Similarly, from the 12 test images, we delineated the nuclei and cytoplasm of 41 isolated cervical cells. Using these cell images, we constructed a synthetic training and test images with the following properties: 1) size of 512×512 pixels, 2) background formed using the

background pixels randomly selected from any of the EDF images, 3) between 2 and 10 different cells, and 4) each cell must overlap at least one cell in the same image with an overlap coefficient in one of the following ranges: $[0, 0.1]$, $[0.1, 0.2]$, $[0.2, 0.3]$, $[0.3, 0.4]$, $[0.4, 0.5]$. Here, the overlap coefficient is defined as $max(\frac{|A \bigcap B|}{|A|}, \frac{|A \bigcap B|}{|B|})$, with A and B representing the regions within the delineation of both cells and $|.|$ denoting the area of the region. In order to create these synthetic images, we first take a patch of background pixels from any of the EDF images, and place it in the 512×512 image, using mirror transformations to smooth the transitions among the background pixels. Then, we pick one of the cells from the training/test set, apply a random rigid geometric transform (translation, rotation from $(0, 2\pi)$ and scale from $(0.8, 1.2)$) and random linear brightness transform and place it on the synthetic image, using a random value (from 0.88 to 0.99) for the alpha channel to simulate the partial transparency effect observed in real EDF cytology images. The next step consists of adding new cells to the image at random locations, where each of these new cells overlaps with at least one of the cells already present in the image and the overlap coefficient is within the range considered for that subset of images. Using the test set, we build 45 subsets of test images with the nine different numbers of cells (i.e., from 2 to 10 cells) and five overlap ranges, as shown in Table IV. Note that these images vary in appearance and segmentation difficulty as a function of the number of cells and degree of overlap (see Fig. 5(a)). We generate 20 images for each of these 45 subsets, giving a synthetic testing database of 900 overlapping cell images. A training set of 45 overlapping cell images is similarly built, but with the training images, we randomly selected 15 images for the training process. This training set is used to define the values of the parameters β, κ, χ in our optimization functions (1), (4) and (7) (see Table II).

In addition, we also performed a quantitive evaluation on a subset of five real EDF images, which have both cytoplasm and nucleus boundaries manually annotated. A comparison of the results between the synthetic and real images is shown in Table II. However, the annotation of real cervical cytology images is a time-consuming and potentially error-prone, which limits the number of images that could be fully annotated at this time.

Quantitative performance is then assessed using the average Dice Coefficient (DC), measured as $DC = 2\frac{|A \bigcap B|}{|A|+|B|}$ over the "good" cell segmentations [36], where a "good" segmentation is considered to be one with a DC above a specific threshold. Here we evaluate performance over the following range of DC thresholds: $\{0.6, 0.7, 0.8, 0.9\}$. We also report the object based false negative rate (FN_o) obtained as the proportion of cells having a DC below this threshold. In addition, we show a pixel-based evaluation using the true positive rate (TP_p) and false positive rate (FP_p) for both training and test sets using the "good" cell segmentations.

Finally, we also compare our nuclei detection methodology with that of Aksoy et al. using the same criteria reported in [8]. Specifically, first we compute the precision and recall of nuclei detection by considering the detection region A and (ground-truth) annotation B, and noting that a correct detection

is represented by $(A \bigcap B)/A > \tau$ and $(A \bigcap B)/B > \tau$, where $\tau = 0.6$. Second, we compute the pixel-based precision and recall values of the correct detections using the Dice Coefficient [8].

Ideally, we would like to compare our overlapping cell segmentation with other approaches available from the literature, but as observed by Plissiti and Nikou [29] this is a largely unexplored area of research. To the best of our knowledge, the only method present in the literature is the one by [2], but we cannot reproduce it reliably with the description presented in that paper. Moreover, other overlapping cell segmentation methodologies [40], [30] need to be substantially extended to work with Pap Smear images. Therefore, we decided to present our results and compare them with those of our preliminary version [20]. We shall also have the training and test databases and our methodology publicly available such that a fair comparison with other methodologies is enabled in this field.

V. EXPERIMENTAL RESULTS

We first show the influence of the parameters κ, χ in the unary and binary terms (4), (7) over the training and test sets of synthetic images. The time step Δt is set as 5, the width of the Dirac Delta function $\epsilon = 1.5$ and the parameter μ is fixed at $0.2/\Delta t = 0.04$ per time step to fulfill the Courant-Friedrichs-Lewy (CFL) condition that $\mu \Delta t < \frac{1}{4}$, as suggested in [19]. We assess the sensitivity of our methodology to the time step Δt and width of the Dirac Delta function ϵ, and we note that the segmentation accuracy does not vary significantly with respect to these two variables (we show the results in the supplementary document). In addition, a relatively large $\Delta t > 1$ can reduce the number of iterations of level set evolution while maintaining numerical accuracy. The parameter β is fixed at 5 since this is the value that produces the best result in the training set. The DC and corresponding FN_o, TP_p and FP_p for each parameter combination on the training set are shown in Table II. This table also shows the results on the test set and real EDF images using the best parameter combination obtained on the training set ($\kappa = 13$, $\chi = 3$). It shows that the algorithm's performance is largely robust to the specific parameters values, but (as expected) performance is better on the training set than on the test set. This is especially the case for FN_o which gets significantly worse on the test set, i.e., by around 0.2 in each case. Table II also shows the pixel-based TP_p and FP_p on the training and test sets for the "good" segmentations (DC > $\{0.6, 0.7, 0.8, 0.9\}$), which show typical TP_p over 0.9 and FP_p approaching zero. In addition, it shows that as the "good" segmentation threshold increases, both DC and FN_o increase. This clearly illustrates the trade-off between the detection of cellular objects and their accurate segmentation. It also demonstrates that our results on the synthetic images are indicative of those that can be expected on real cervical cytology images.

Table III shows a comparison of the performance of the algorithm described in this paper with that of the previous version of this algorithm [20]. These results were obtained using the test database described in [20] and show a consistent improvement in performance for both DC and TP_p with either no detriment, or slight improvements in FP_o and FP_p.

Next, using the parameters that produced the best results on the training data (i.e., $\kappa = 13$, $\chi = 3$ as shown in Table II), we compute DC, FN_o, TP_p and FP_p on the test set of synthetic images for a "good" segmentation threshold of $DC > 0.7$. These results are presented in Table IV as a function of the number of cells and pairwise overlap coefficient. A graphical visualization of Table IV is depicted in Fig. 4. These results show that our methodology can successfully segment cell clumps with a large number of cells (between 8 and 10 cells) provided the overlap between pairs of cells is relatively low (between 0.1 and 0.2). Furthermore, if the clump has a small number of cells (between two and three cells), our methodology can successfully segment the cells even when the overlap coefficient is between 0.4 and 0.5. Six typical segmentations for a differing number of cells and degree of cell overlap are shown in Fig. 5 (a), where we show not only the automated detection, but also the ground truth. A visual inspection of these results verify the quantitative results presented in Table IV. Fig. 5 (b) shows four of the real EDF images in the dataset. While these segmentations contain a number of false nuclei detections and are unlikely to perfectly delineate each cell's cytoplasm, they demonstrate the efficacy of our proposed approach on field of view images of real-world cytological specimens. It is also important to mention that our methodology is able to segment 645 cells which is roughly 10 times more than the initial 53 free-lying cells present in these 16 EDF images. Note that a larger set of visual results for both the synthetic and real images are shown in the supplementary material.

Moreover, we compare our nuclei detection with the approach by [8]. However, this comparison is not ideal as they are run on different data sets as the database in [8] is not publicly available. Specifically, Aksoy et al.'s approach is tested on Hacettepe data set (which has 139 nuclei), while ours are the EDF cytology images described above (with 645 nuclei). In terms of object-based nuclei detection, we achieve an equivalent precision of 0.73, but with a slightly worse recall of 0.85, as compared to [8] which report a precision of 0.74 and recall 0.93. Furthermore, the pixel-based results for our method are slightly better consisting of a precision of 0.96($\pm$.06), recall 0.90($\pm$.08) and Dice 0.92($\pm$.05); while [8] has a precision of 0.91($\pm$.08), recall 0.88($\pm$.07) and Dice 0.89 ($\pm$.04).

Finally, the average running time of our algorithm on the synthetic images is reported in Fig. 6 as a function of the number of cells and cell overlap. This figures have been obtained using an un-optimized Matlab code on a PC with 2.66 GHz Intel Core 2 Duo processor and 8 GB RAM.

VI. DISCUSSION

The unary and binary terms, weighted by κ and χ in the optimization functions (4), (7) are shown to be important, according to the results in Table II. Nevertheless it is important to notice that the regularization term in (5) alone produces competitive results, which can be attributed to the reliable

TABLE II

QUANTITATIVE EVALUATION (MEAN AND STANDARD DEVIATION IN BRACKETS) SHOWING THE INFLUENCE OF THE LEVEL SET PARAMETERS IN THE TRAINING PROCESS AND TEST RESULTS (BOTH REAL EDF IMAGES & SYNTHETIC TESTING IMAGES) IN TERMS OF THE DC, FN_o, TP_p AND FP_p FOR "GOOD" SEGMENTATIONS (EACH COLUMN SHOWS A DIFFERENT CRITERION FOR A "GOOD" SEGMENTATION).

κ	χ	DC$>$ 0.6	DC$>$ 0.7	DC$>$ 0.8	DC$>$ 0.9
		Training set			
0	0	DC=.89(.09),FN_o=.08(.15) TP_p=.93(.09),FP_p=.01(.01)	DC=.90(.08),FN_o=.10(.16) TP_p=.94(.07),FP_p=.01(.01)	DC=.93(.05),FN_o=.26(.22) TP_p=.95(.04),FP_p=.01(.01)	DC=.95(.02), FN_o=.48(.24) TP_p=.95(.04),FP_p=.00(.00)
0	3	DC=.87(.09),FN_o=.12(.19) TP_p=.83(.13),FP_p=.00(.00)	DC=.90(.06),FN_o=.19(.23) TP_p=.85(.10),FP_p=.00(.00)	DC=.91(.04),FN_o=.28(.27) TP_p=.87(.08),FP_p=.00(.00)	DC=.94(.03), FN_o=.61(.36) TP_p=.92(.06),FP_p=.00(.00)
13	0	DC=.89(.09),FN_o=.08(.15) TP_p=.93(.10),FP_p=.01(.01)	DC=.90(.08),FN_o=.10(.16) TP_p=.94(.07),FP_p=.01(.01)	DC=.92(.05),FN_o=.24(.22) TP_p=.95(.04),FP_p=.01(.01)	DC=.95(.02), FN_o=.46(.23) TP_p=.95(.04),FP_p=.00(.00)
13	3	DC=.90(.08),FN_o=.09(.15) TP_p=.91(.10),FP_p=.01(.01)	DC=.91(.07),FN_o=.11(.17) TP_p=.91(.08),FP_p=.01(.01)	DC=.92(.05),FN_o=.18(.22) TP_p=.92(.06),FP_p=.00(.00)	DC=.95(.03), FN_o=.44(.28) TP_p=.93(.05),FP_p=.00(.00)
		Test set			
13	3	DC=.87(.10),FN_o=.24(.27) TP_p=.89(.11),FP_p=.00(.01)	DC=.89(.08),FN_o=.31(.29) TP_p=.90(.10),FP_p=.00(.00)	DC=.92(.06),FN_o=.43(.31) TP_p=.92(.08),FP_p=.00(.00)	DC=.96(.03), FN_o=.63(.33) TP_p=.95(.05),FP_p=.00(.00)
		Five real EDF images			
13	3	DC=.84(.11),FN_o=0.26(.07) TP_p=.88(.12),FP_p=.00(.00)	DC=.87(.09),FN_o=.36(.08) TP_p=.90(.10),FP_p=.00(.00)	DC=.91(.06),FN_o=.53(.06) TP_p=.91(.08),FP_p=.00(.00)	DC=.96(.03),FN_o=.72(.08) TP_p=.94(.04),FP_p=.00(.00)

TABLE III

QUANTITATIVE COMPARISON AGAINST THE PREVIOUS VERSION OF OUR METHODOLOGY [20] ON THE TEST SET OF [20], AND THE SUBSET OF REAL EDF IMAGES (USING THE MEAN AND STANDARD DEVIATION RESULT OF EACH MEASURE).

Our result			
DC$>$ 0.6	DC$>$ 0.7	DC$>$ 0.8	DC$>$ 0.9
DC=.93(.08),FN_o=.00(.00) TP_p=.95(.07),FP_p=.004(.01)	DC=.94(.07),FN_o=.02(.06) TP_p=.95(.07),FP_p=.004(.01)	DC=.96(.03),FN_o=.11(.15) TP_p=.96(.04),FP_p=.002(.004)	DC=.97(.02), FN_o=.17(.19) TP_p=.96(.04),FP_p=.001(.002)
Result from our previous approach [20]			
DC=.90(.08),FN_o=.02(.09) TP_p=.88(.11),FP_p=.003(.01)	DC=.90(.08),FN_o=.02(.09) TP_p=.88(.11),FP_p=.003(.01)	DC=.92(.05),FN_o=.13(.18) TP_p=.89(.09),FP_p=.002(.004)	DC=.95(.02), FN_o=.38(.26) TP_p=.94(.03),FP_p=.001(.002)

TABLE IV

RESULTS (MEAN AND STANDARD DEVIATION IN BRACKETS) ON THE TEST SET IN TERMS OF THE DC, FN_o, TP_p AND FP_p FOR "GOOD" SEGMENTATIONS WITH $DC > 0.7$, AS A FUNCTION OF THE NUMBER OF CELLS.

	Overlap $\in [0, 0.1]$	Overlap $\in [0.1, 0.2]$	Overlap $\in [0.2, 0.3]$	Overlap $\in [0.3, 0.4]$	Overlap $\in [0.4, 0.5]$
2 cells	DC=.98(.02),FN_o=.1(.3) TP_p=.99(.03),FP_p=.00(.00)	DC=.92(.06),FN_o=.1(.2) TP_p=.93(.05),FP_p=.00(.00)	DC=.92(.06),FN_o=.1(.3) TP_p=0.92(.07),FP_p=.00(.00)	DC=.91(.06), FN_o=.2(.4) TP_p=.89(.11),FP_p=.00(.00)	DC=.88(.06), FN_o=.1(.3) TP_p=.89(.09),FP_p=.00(.00)
3 cells	DC=.98(.02),FN_o=.1(.3) TP_p=.99(.03),FP_p=.00(.00)	DC=.90(.07),FN_o=.1(.3) TP_p=.90(.08),FP_p=.00(.00)	DC=.88(.07),FN_o=.2(.3) TP_p=.89(.09),FP_p=.00(.00)	DC=.88(.07), FN_o=.3(.4) TP_p=.90(.09),FP_p=.00(.01)	DC=.87(.08), FN_o=.3(.3) TP_p=.88(.11),FP_p=.00(.00)
4 cells	DC=.98(.03),FN_o=.2(.2) TP_p=.98(.03),FP_p=.00(.00)	DC=.90(.07),FN_o=.1(.2) TP_p=.90(.07),FP_p=.00(.00)	DC=.86(.08),FN_o=.2(.3) TP_p=.88(.09),FP_p=.00(.01)	DC=.88(.07), FN_o=.3(.3) TP_p=.90(.10),FP_p=.00(.01)	DC=.85(.07), FN_o=.4(.3) TP_p=.88(.10),FP_p=.01(.00)
5 cells	DC=.98(.02),FN_o=.2(.1) TP_p=.98(.03),FP_p=.00(.00)	DC=0.89(.07),FN_o=.2(.3) TP_p=.90(.08),FP_p=.00(.01)	DC=.88(.07),FN_o=.2(.3) TP_p=.89(.09),FP_p= .00(.00)	DC=.86(.07), FN_o=.4(.4) TP_p=.89(.10),FP_p=.01(.01)	DC=.84(.07), FN_o=.3(.3) TP_p=.87(.11),FP_p=.01(.01)
6 cells	DC=.98(.03),FN_o=.1(.2) TP_p=.97(.04),FP_p=.00(.00)	DC=.88(.08),FN_o=.1(.2) TP_p=.88(.10),FP_p=.00(.00)	DC=.87(.07),FN_o=.3(.3) TP_p=.88(.11),FP_p=.00(.00)	DC=.85(.08), FN_o=.4(.3) TP_p=.88(.12),FP_p=.01(.01)	DC=0.85(.07), FN_o=.5(.3) TP_p=.87(.09),FP_p=.01(.01)
7 cells	DC=.98(.04),FN_o=.2(.1) TP_p=.98(.04),FP_p=.00(.00)	DC=.89(.07),FN_o=.2(.3) TP_p=.89(.09),FP_p=.00(.00)	DC=.87(.08),FN_o=.2(.2) TP_p=0.88(.09),FP_p=.00(.01)	DC=.84(.07), FN_o=.5(.3) TP_p=0.88(.10),FP_p=.01(.01)	DC=.85(.07), FN_o=.5(.2) TP_p=0.87(.11),FP_p=.01(.01)
8 cells	DC=.97(.04),FN_o=.1(.1) TP_p=.97(.05),FP_p=.00(.00)	DC=.89(.07),FN_o=.3(.2) TP_p=.91(.07),FP_p=.00(.00)	DC=.85(.06),FN_o=.3(.2) TP_p=.86(.11),FP_p=.01(.01)	DC=.84(.07), FN_o=.5(.2) TP_p=.87(.10),FP_p=.01(.01)	DC=.83(.08), FN_o=.5(.2) TP_p=.85(.12),FP_p=.01(.01)
9 cells	DC=.97(.04),FN_o=.1(.1) TP_p=.96(.05),FP_p=.00(.00)	DC=.88(.07),FN_o=.2(.2) TP_p=.89(.09),FP_p=.00(.00)	DC=0.85(.08),FN_o=.3(.2) TP_p=0.87(.11),FP_p=.00(.00)	DC=.85(.07), FN_o=.5(.2) TP_p=.86(.10),FP_p=.00(.01)	DC=.84(.07), FN_o=.7(.2) TP_p=.85(.12),FP_p=.01(.01)
10 cells	DC=.95(.06),FN_o=.1(.1) TP_p=.95(.06),FP_p=.00(.00)	DC=.88(.08),FN_o=.2(.2) TP_p=.88(.10),FP_p=.00(.00)	DC=.85(.08),FN_o=.4(.2) TP_p=.87(.10),FP_p=.00(.01)	DC=.85(.08), FN_o=.5(.2) TP_p=.86(.11),FP_p=.00(.00)	DC=.83(.07), FN_o=.6(.2) TP_p=.86(.11),FP_p=.01(.01)

initializations for each level set function produced by our methodology. Another important point worth mentioning is the small gap between the training and test set results, with the exception of the relatively larger FN_o. This larger FN_o results are mostly due to the false negative nucleus detection, where most of the nuclei that were not detected are represented by light black spot in their appearance and have blur transition to the cytoplasm, which makes the MSER algorithm fail. Compared to our previous methodology [20], we notice in Table III that the methodology proposed in this paper shows significant improvements in all of the performance measures.

The qualitative results obtained from visual inspection of the segmentation on the synthetic and real EDF images, shown in Fig. 5(b), allow us to conclude that our methodology produces robust results even on challenging images containing large clumps of cells. Also, the use of our segmentation algorithm produces 10 times more cells from the 16 EDF images than current methodologies that only segment free-lying cells. Finally, our nuclei detection produces quantitative results on par with the state-of-the-art [8].

The methodology proposed in this paper produces robust results on the problem of segmenting both nuclei and cyto-
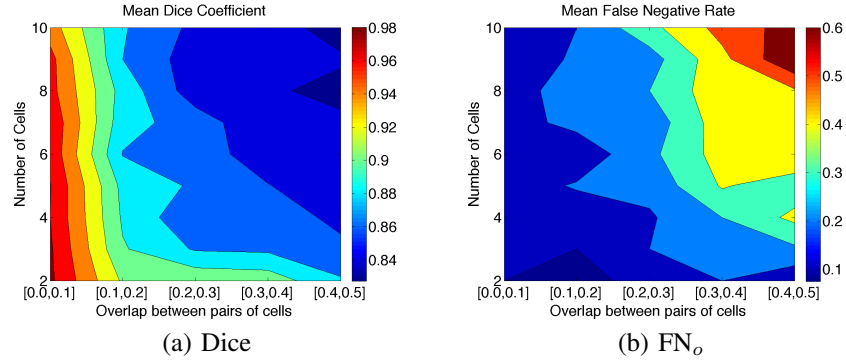
(a) Dice　　　　　　　　　　　　　　　　(b) FN$_o$

Fig. 4. Mean Dice coefficient (a) and object based false negative rate (b) as a function of number of cells and overlap ratio. This is a visualization of the results in Table IV.

(a) Synthetic images (automated detection on top, and ground truth on bottom)
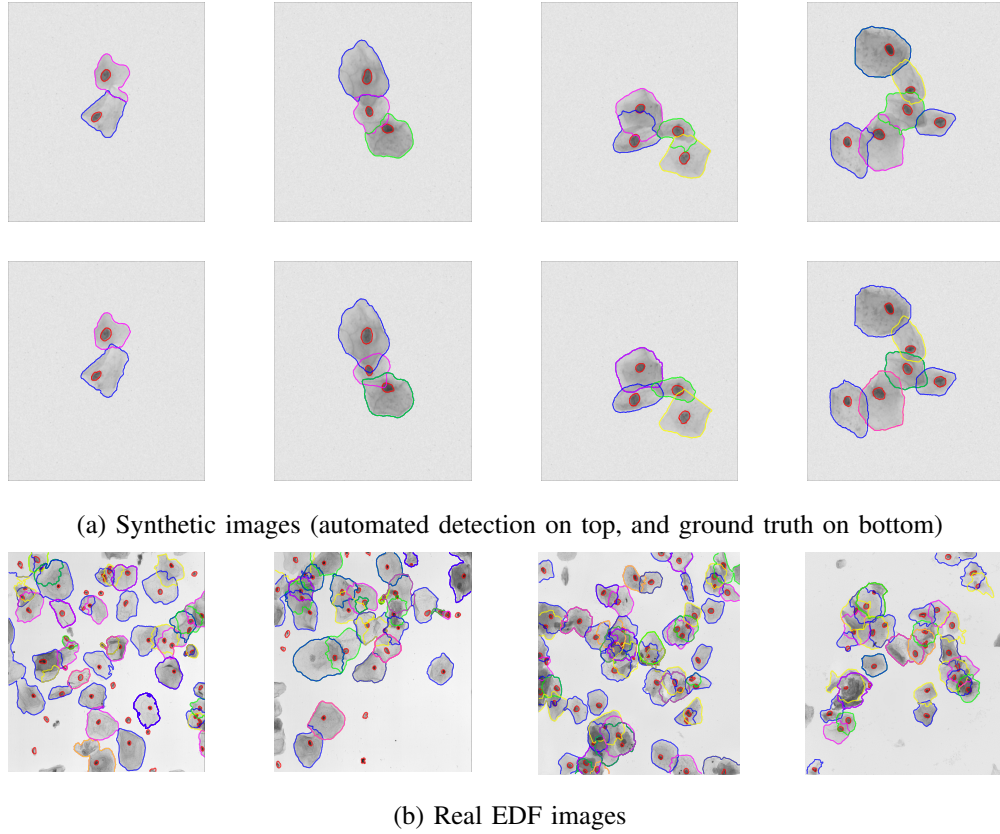

(b) Real EDF images

Fig. 5. Segmentation results on the synthetic images (a) and real EDF images (b).

plasm from overlapping cervical cells. There are a few issues we have encountered, such as the lack of precision when segmenting cells embedded in clumps with a large number of cells and a large overlap between cells. Another issue is when one of the cells to be segmented does not present a significant proportion of its border in the clump boundary. This issue causes a failure in the estimation of the shape prior based on geometric constraints (Sec. III-B3), which cannot produce the initial segmentation, the unary (1) and the binary constraints (2) for that cell. Furthermore, the false negative detection of nuclei is another issue, as previously explained. One last issue is the slow running time of the algorithm, which is severely affected by the interpolation used in the computation of the

shape prior for each cell, as described in (1) and (2).

There are a few points that need to be addressed to improve the effectiveness of our approach. For instance, the level set method we use is based on the classic level set method [24] that has issues with the initial segmentation and the re-initialization of the distance function. The issue related with the re-initialization of the distance function has been dealt with by a method proposed by [19], which is the level set method used in our paper, but we still need to provide good initial segmentations for the level set functions representing the detection of each cell. Nevertheless, the more recent proposal of [5] has introduced a global optimizer for the level set method that addresses both of these issues, and we plan to
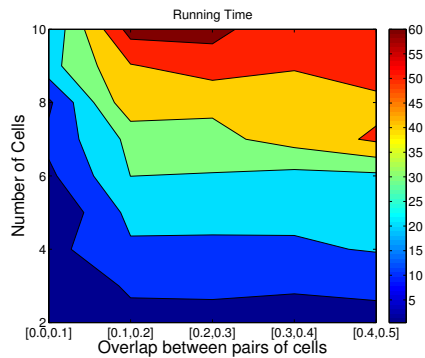
Fig. 6. Running time (in minutes) of our algorithm on the synthetic images.

adapt this method to our problem. Another improvement that can be applied in our approach is an extension to further refine segmentation results based on information in the original stack of multi-focal plane images (see Sec. IV) as per the manual cervical cell analysis. In addition, we have only tested the algorithm on normal appearing cervical cytology images and different levels of difficulty by varying both number of cells and their degree of overlap. However, abnormal cervical cells can have quite a different appearance, with enlarged nuclei and more varied shape indicative of their disease state. Therefore, further work should also adapt the system and test images to process both normal and abnormal cells by modifying the nuclei detection strategy and shape prior.

Automation in the analysis of various types of cytology specimens is both desirable and ongoing [47] [48]. The algorithm proposed here is suitable for extension to other types of cytological cells such as buccal and breast fine-needle-aspirates [46]. This is likely to be fairly straightforward, provided there is reliable prior knowledge of the nucleus-cytoplasm structure. Without this information, it is likely that the effectiveness of the methodology will be severely compromised. This is because, in our method, the cytoplasm segmentation is underpinned by the accuracy of the initial segmentation of the LSF, which is extrapolated using the boundaries of the clumps of overlapping cells and the detected nuclei produced by the initial scene segmentation. For example, MSER-based nuclei detection method cannot readily detect cells from microscopic fluorescence images, which contain a large number of bright spots with no nucleus-cytoplasm structure. In future, we would like to generalise the cell detection function of the algorithm to make it more readily adaptable to a variety of cell types and depositions.

VII. CONCLUSIONS

In this paper we have presented an algorithm that addresses the challenging problem of segmenting each individual cell's nucleus and cytoplasm from a clump of cervical cells deposited on a microscope slide. The method is based on a joint optimisation of several level set functions and is demonstrated to perform well on clumps of up to 10 cells, provided the overlap between pairs of cells is below 0.2. In addition, if the clump consists of three or fewer cells, then our methodology

can successfully segment individual cells when the overlap is a large as 0.5. These results hold the promise that the automated analysis of cervical cytology specimens can be improved via a more complete analysis of a larger subset of the cells present on each cytology specimen.

ACKNOWLEDGMENT

REFERENCES

[1] Aubert, G. and Kornprobst, P. : Mathematical Problems in Image Processing: Partial Differential Equations and the Calculus of Variations. New York: Springer-Verlag (2002)
[2] Béliz-Osorio, N., Crespo, J., García-Rojo, M., Muñoz, A., Azpiazu, J.: Cytology imaging segmentation using the locally constrained watershed transform. Mathematical Morphology and Its Applications to Image and Signal Processing, (2011) 429-438.
[3] Bishop J., Bigner S., Colgan T., Husain M., Howell L., McIntosh K., Taylor D., Sadeghi M.: Multicenter Masked Evaluation of AutoCyte PREP Thin Layers with Matched Conventional Smears. Acta Cytologica, 42, (1998) 189-197.
[4] Bradley, A., Bamford, P.: A one-pass extended depth of field algorithm based on the over-complete discrete wavelet transform. Image and Vision Computing 'New Zealand (IVCNZ), (2004) 279-284
[5] Bresson, X., Esedoglu, S., Vandergheynst, P., Thiran, J. P., and Osher, S.: Fast global minimization of the active contour/snake model. Journal of Mathematical Imaging and vision, 28(2), (2007) 151-167.
[6] Comaniciu, D., Meer, P.: Mean shift: a robust approach toward feature space analysis. IEEE TPAMI, 24(5) (2002) 603-619.
[7] Dillencourt, Michael B., Hannan Samet, and Markku Tamminen. A general approach to connected-component labeling for arbitrary image representations. Journal of the ACM (JACM) 39, no. 2 (1992) 253-280.
[8] Gençtav, A., Aksoy, S., Önde, S.: Unsupervised segmentation and classification of cervical cell images. Pattern Recognition, Vol. 45 (2012) 4151-4168.
[9] Grohs, H., et al.: Standardization of specimen preparation through mono/thin-layer technology. in H. K. Grohs and O. A. N. Husain, eds, Automated Cervical Cancer Screening. IGAKU-SHOIN Medical Publishers, New York (1994).
[10] C. Jung and C. Kim, Segmenting clustered nuclei using H-minima transform-based marker extraction and contour parameterization. IEEE TBE, 57(10), (2010) 2600-2604.
[11] Jung, C., Kim, C., Chae, S., Oh, S.: Unsupervised segmentation of overlapped nuclei using bayesian classification. IEEE TBE, 57(12), (2010) 2825-2832.
[12] Kale, A., Aksoy, S.: Segmentation of cervical cell images. ICPR, Istanbul, Turkey. (2010) 2399-2402.
[13] Li, K., Lu, Z., Liu, W., Yin, J.: Cytoplasm and nucleus segmentation in cervical smear images using Radiating GVF Snake. Pattern Recognition, Vol. 45 (2012) 1255-1264.
[14] Zhang, L., Kong, H., Chin, C., Liu, S., Chen, Z., Wang, T., Chen, S.: Segmentation of cytoplasm and nuclei of abnormal cells in cervical cytology using global and local graph cuts. Computerized Medical Imaging and Graphics, Vol. 38 (2014) 369-380.
[15] Gao, X., Wang, B., Tao, D., Li, X.: A relay Level Set method for automatic image segmentation. IEEE Transactions on Systems, Man, and Cybernetics, Part B: Cybernetics, Vol. 41 (2011) 518-525.
[16] Wang, B., Gao X., Tao, D., Li, X.: A unified tensor Level Set for image segmentation. IEEE Transactions on Systems, Man, and Cybernetics, Part B: Cybernetics, Vol. 40 (2010) 857-867.
[17] Dambreville, S., Rathi, Y., Tannenbaum, A.: A framework for image segmentation using shape models and kernel space shape priors. IEEE Transactions on Pattern Analysis and Machine Intelligence, Vol. 30 (2008) 1385-1399.
[18] Chen, F., Yu, H., Hu, R., Zeng, X.: Deep learning shape priors for object segmentation. CVPR (2013) 1870-1877.
[19] Li, C., Xu, C., Gui, C., Fox, M.: Distance regularized level set evolution and its application to image segmentation. IEEE TIP, 19(12) (2010) 3243-3254.

[20] Lu, Z., Carneiro, G., Bradley, A.: Automated nucleus and cytoplasm segmentation of overlapping cervical cells. MICCAI (2013) 452-460.

[21] Matas, J., Chum, O., Urban, M., Pajdla, T.: Robust wide baseline stereo from maximally stable extremal regions. In Proc. BMVC, Cardiff, UK. (2002) 384-396.

[22] Meijering, E.: Cell Segmentation: 50 Years Down the Road. Signal Processing Magazine, IEEE 29, no. 5 (2012) 140-145.

[23] Noorani, H.: Assessment of techniques for cervical cancer screening. CCOHTA 1997: 2E, Canadian Coordinating Office for Health Technology Assessment. (1997).

[24] Osher, S., Sethian, J.: Fronts propagating with curvature-dependent speed: Algorithms based on HamiltonJacobi formulations. J. Comput. Phys. 79(1), 1249 (1988).

[25] Papanicolaou, G.: A new procedure for staining vaginal smears. Science, Vol. 95, no. 2469 (1942) 438-439.

[26] Papillo, J.L., Zarka, M.A., St John, T.L.: Evaluation of the ThinPrep Pap test in clinical practice. Acta Cytologica, Vol. 42, no. 1 (1998) 203-208.

[27] Plissiti, M., Nikou, C., Charchanti, A.: Automated detection of cell nuclei in pap smear images using morphological reconstruction and clustering. IEEE Transactions on Information Technology in Biomedicine, Vol. 15, (2011) 233-241.

[28] Plissiti, M., Nikou, C.: Overlapping cell nuclei segmentation using a spatially adaptive active physical model. IEEE TIP. 21(11) (2012) 4568-4580.

[29] Plissiti, M., Nikou, C.: A Review of Automated Techniques for Cervical Cell Image Analysis and Classification. Biomedical Imaging and Computational Modeling in Biomechanics. Lecture Notes in Computational Vision and Biomechanics Volume 4 (2013) 1-18.

[30] Quelhas, P., Marcuzzo, M., Mendonca, A.M., Campilho, A.: Cell nuclei and cytoplasm joint segmentation using the sliding band filter. IEEE TMI, 29(8) (2010) 1463-1473.

[31] Dufour, A., Shinin, V., Tajbakhsh, S., Guillen-Aghion, N., Olivo-Marin, J.-C., Zimmer, C.: Segmenting and tracking fluorescent cells in dynamic 3-D microscopy with coupled active surfaces. IEEE Transactions on Image Processing, Vol. 14, (2005) 1396-1410.

[32] Qi, X., Xing, F., Foran, D.J., Yang, L.: Robust segmentation of overlapping cells in histopathology specimens using parallel seed detection and repulsive Level Set. IEEE Transactions on Biomedical Engineering, Vol. 59, (2012) 754-765.

[33] Irshad, H., Veillard, A., Roux, L., Racoceanu, D.: Methods for nuclei detection, segmentation, and classification in digital histopathology: a review - current status and future potential. IEEE Reviews in Biomedical Engineering, Vol. 7, (2014) 97-114.

[34] Cloppet, F., Boucher, A.: Segmentation of overlapping/aggregating nuclei cells in biological images. ICPR (2008) 1-4.

[35] Hu, M., Ping, X., Ding, Y.: Automated cell nucleus segmentation using improved snake. ICIP (2004) 2737-2740.

[36] Radau, P., Lu, Y., Connelly, K., Paul, G., Dick, A., Wright, G.: Evaluation framework for algorithms segmenting short axis cardiac MRI. The MIDAS Journal - Cardiac MR Left Ventricle Segmentation Challenge (2009).

[37] Rousson, M., Paragios, N.: Shape priors for level set representations. In: Heyden, Anders and Sparr, Gunnar and Nielsen, Mads and Johansen, Peter (eds.) ECCV 2002. LNCS, Springer, Heidelberg (2002) 78-92.

[38] Schechner, Y., Kiryati, N., Basri, R.: Separation of transparent layers using focus. IJCV. 39(1), Kluwer Academic Publishers (2000) 25-39.

[39] Vedaldi, A., Soatto, S.: Quick Shift and Kernel Methods for Mode Seeking. In: Forsyth, David and Torr, Philip and Zisserman, Andrew (eds.) ECCV 2008. LNCS, Springer, Heidelberg (2008) 705 - 718.

[40] Wahlby, C., Lindblad, J., Vondrus, M., Bengtsson, E., Bj´orkesten, L.: Algorithms for cytoplasm segmentation of fluorescence labelled cells. Analytical Cellular Pathology, 24(3) (2002) 101-111.

[41] Wu, H.-S., Gil, J., Barba, J.: Optimal segmentation of cell images. IEE Proc. on Vision, Image and Signal Processing. Vol. 145 (1998) 50-56.

[42] X. Chenyang Xu and J. Prince, Snakes, shapes, and gradient vector flow, IEEE TIP, Vol. 7 (1998) 359-369.

[43] Yang-Mao, S.-F., Chan, Y.-K., Chu, Y.-P.: Edge enhancement nucleus and cytoplast contour detector of cervical smear images. IEEE Trans. on Systems, Man, and Cybernetics, Part B: Cybernetics, Vol. 38 (2008) 353-366.

[44] Zimmer, C., Olivo-Marin, J-C.: Coupled parametric active contours. IEEE TPAMI, 27(1) (2005) 1838-1842.

[45] Ringaby, E., Friman, O., Forssen, P.-E., Opsahl, T.O., Haavardsholm, T.V., Kasen, I.: Anisotropic Scattered Data Interpolation for Pushbroom Image Rectification. IEEE Transactions on Image Processing, Vol. 23 (2014) 2302-2314.

[46] Bdard, YC., Pollett, AF.: Breast fine-needle aspiration. A comparison of ThinPrep and conventional smears. American journal of clinical pathology, Vol. 111 (1999) 523-527.

[47] Chiu, S. J., Lokhnygina, Y., Dubis, A. M., Dubra, A., Carroll, J., Izatt, J. A., Farsiu, S.: Automatic cone photoreceptor segmentation using graph theory and dynamic programming. Biomedical Optics Express, Vol. 4 (2013) 924-937.

[48] Chiu, S. J., Toth, C. A., Rickman, C. B., Izatt, J. A., Farsiu, S.: Automatic segmentation of closed-contour features in ophthalmic images using graph theory and dynamic programming. Biomedical Optics Express, Vol.3 (2012) 1127-1140.

[49] Caselles, V., Kimmel, R., Sapiro, G.: Geodesic Active Contours. International Journal of Computer Vision, Vol. 22 (1997) 61-79.

[50] Yang, X., Gao, X., Li, J., Han, B.: A shape-initialized and intensity-adaptive level set method for auroral oval segmentation. Information Sciences, 277 (2014) 794-807.

[51] Yang, X., Gao, X., Tao, D., Li, X.: Improving Level Set Method for Fast Auroral Oval Segmentation. IEEE Transactions on Image Processing, Vol. 23 (2014) 2854-2865.

Zhi Lu received the Ph.D degree in computer science from City University of Hong Kong, Hong Kong, China, in 2014. Previously, Dr. Zhi Lu received his M.Sc. and M.Phil. degrees in computer science from the same university in 2008 and 2011, respectively. Currently, he is a postdoctoral researcher at the School of Computer Science of the University of Adelaide in Australia. His research interests include medical image analysis and pattern recognition.

Gustavo Carneiro received his BS and MSc degrees in computer science from the Federal University of Rio de Janeiro, and the Military Institute of Engineering, Brazil, in 1996 and 1999, respectively. Dr. Carneiro received his PhD degree in Computer Science from the University of Toronto, Canada, in 2004. Currently he is an associate professor at the School of Computer Science of the University of Adelaide in Australia. Previously, Dr. Carneiro worked at the Instituto Superior Tecnico (IST), Technical University of Lisbon from 2008 to 2011 as a visiting researcher and assistant professor, and from 2006-2008, he worked at Siemens Corporate Research in Princeton, USA. He was the recipient of a Marie Curie International Incoming Fellowship and has authored more than 50 peer-reviewed publications in international journals and conferences. His research interests include medical image analysis, image feature selection and extraction, content-based image retrieval and annotation, and general visual object classification.

Andrew P. Bradley received his Ph.D. from The University of Queensland in 1996. He was then a Post-doctoral Fellow at The University of Alberta, a Principal Research Engineer with Canon Information Systems Research Australia and a Senior Lecturer at The University of New South Wales. He has twice been a visiting research fellow at BT Exact Technologies in the UK and has been retained as a project consultant by a number of Australian companies. He is currently Professor in Biomedical Engineering at The University of Queensland. He is a Senior Member of the IEEE.